



HAL
open science

Paradigm shift of platinum oxidation below fuel cell open-circuit voltage

Raphaël Chattot, Carlos Campos-Roldàn, Amir Gasmi, Morgane Stodel, Isaac Martens, Jean-Sébastien Filhol, Jakub Drnec, Pierre-Yves Blanchard, Sara Cavaliere, Deborah Jones

► **To cite this version:**

Raphaël Chattot, Carlos Campos-Roldàn, Amir Gasmi, Morgane Stodel, Isaac Martens, et al..
Paradigm shift of platinum oxidation below fuel cell open-circuit voltage. 2024. hal-04773732

HAL Id: hal-04773732

<https://hal.science/hal-04773732v1>

Preprint submitted on 8 Nov 2024

HAL is a multi-disciplinary open access archive for the deposit and dissemination of scientific research documents, whether they are published or not. The documents may come from teaching and research institutions in France or abroad, or from public or private research centers.

L'archive ouverte pluridisciplinaire **HAL**, est destinée au dépôt et à la diffusion de documents scientifiques de niveau recherche, publiés ou non, émanant des établissements d'enseignement et de recherche français ou étrangers, des laboratoires publics ou privés.



Distributed under a Creative Commons Attribution 4.0 International License

Paradigm shift of platinum oxidation below fuel cell open-circuit voltage

Raphaël Chattot

raphael.chattot@umontpellier.fr

ICGM <https://orcid.org/0000-0001-6169-530X>

Carlos Campos-Roldàn

ICGM

Amir Gasmi

University of Montpellier

Morgane Stodel

University of Toulouse III

Isaac Martens

European Synchrotron Radiation Facility <https://orcid.org/0000-0001-8342-6629>

Jean-Sébastien Filhol

ICGM

Jakub Drnec

European Synchrotron Radiation Facility

Pierre-Yves Blanchard

ICGM

Sara Cavaliere

ICGM

Deborah Jones

Université Montpellier

Article

Keywords: fuel cells, heterogeneous catalysis, platinum oxidation, durability, stroboscopic operando X-ray scattering

Posted Date: September 28th, 2023

DOI: <https://doi.org/10.21203/rs.3.rs-3366519/v1>

License: © ⓘ This work is licensed under a Creative Commons Attribution 4.0 International License.

[Read Full License](#)

Additional Declarations: There is **NO** Competing Interest.

Abstract

The long-term stability of Pt catalysts is critical to the reliability of proton exchange membrane fuel cells (PEMFCs), and receives constant attention. However, the current knowledge of Pt oxidation is restricted to unrealistic PEMFC cathode environment or operation, which questions its practical relevance.

Herein, Pt oxidation is investigated directly in a PEMFC with stroboscopic *operando* high energy X-ray scattering. The critical potential for the Pt-O dipole place-exchange mechanism is observed far below the previously reported value, and most importantly, below the open-circuit potential of PEMFC cathode. Such early oxidation is shown to control PEMFC performance and its role on Pt transient dissolution is verified by electrochemical on-line inductively coupled plasma mass spectrometry. By further demonstrating and resolving the limitations of currently employed accelerated stress test protocols in the light of place-exchange time constants, this new paradigm of Pt oxidation paves the way to new mitigation strategies against PEMFC degradation.

TEXT

The durability of proton exchange membrane fuel cells (PEMFCs), notably for transport applications, largely depends on the long-term stability of the costly cathodic platinum-based state-of-the-art electrocatalyst¹⁻⁵. The highly corrosive environment of the cathode, where the oxygen reduction reaction (ORR) occurs, challenges the (electro)chemical stability range of most of metals, even as noble as Pt⁶. This is especially true for nanoparticulate Pt under dynamic load profiles, and is magnified during particular events such as hydrogen fuel starvation or during PEMFC start-up and shut-down. During such events the cathode potential was shown to possibly exceed the open-circuit potential (OCP) of typically 1.0 V vs. the reversible hydrogen electrode (RHE), depending on the oxidant gas composition⁷⁻⁹. Tremendous research efforts have been dedicated to the elucidation of Pt catalyst degradation mechanisms above the OCP, which are now largely understood notably thanks to the recent development of *in situ* and *operando* characterization techniques. Among them, studies on model Pt single crystal electrodes and commercial carbon-supported Pt electrocatalysts (Pt/C) using (surface) X-ray diffraction¹⁰⁻¹⁷, and/or electrochemical on-line inductively coupled plasma mass spectrometry (ICP-MS)^{16,18-21} provided evidenced for distinct mechanisms for Pt dissolution. Under dynamic potential (or load) profiles, Pt dissolution was found to be mostly a transient process, triggered by both Pt oxide formation (anodic dissolution) and subsequent Pt oxide reduction (cathodic dissolution). A general observation from the aforementioned studies is that significant transient Pt dissolution starts only at specific potentials above the OCP (*ca.* 1.05 - 1.10 V vs. RHE, depending on Pt surface structure), which trigger Pt-O dipole inversion by the place-exchange mechanism²². In contrast, at constant electrode potential (*i.e.* at the steady-state when the Pt surface is in equilibrium), the chemical dissolution of Pt or Pt oxide was highlighted as being only a minor path of Pt dissolution, both above and below the OCP^{23,24}. From such observations, it was concluded that under conventional PEMFC operation

(*i.e.* below the OCP), 4.8 nm Pt/C catalysts should largely exceed 5,000 h lifetime with only one Pt monolayer dissolved^{24,25}. This is, however, not validated in practice⁴.

It must be stated that these conclusions were derived from model *in situ* or *operando* experiments strictly involving a combination of either (i) the use of model catalyst materials (single-crystal electrodes or thin-film catalyst layers), (ii) the use of an electrochemical environment different from that in a PEMFC (weakly-adsorbing aqueous electrolyte) and/or (iii) the use of unrealistic PEMFC operating conditions (such as room temperature or cathode potential range as large as 0.05 - 1.50 V vs. RHE, mostly restricted to reactant gas starvation, or PEMFC start-up/shut-down cases). As argued by Đukić *et al.*²⁶, those deviations from usually encountered operation conditions are of primary importance considering the high dependence of Pt dissolution on such experimental parameters. It is thus still largely unclear how this knowledge of Pt oxidation and dissolution for very exceptional cases actually apply to the practical PEMFC during most of its lifetime, *i.e.* for cathode potentials below or at the OCP.

This work aims at providing a pragmatic description of state-of-the-art Pt nanocatalyst oxidation and dissolution dynamics in conditions directly relevant to PEMFC cathode application. The previously demonstrated ability of high energy wide-angle X-ray scattering (WAXS) in revealing nanocatalyst oxidation trends *operando*^{14,27,28} is here supported by theoretical calculations and pushed significantly further by employing a stroboscopic measurement strategy allowing the acquisition of ultra-fast data with high signal quality and temporal resolution. The observed trends in Pt oxidation, notably regarding the underestimated extent of place-exchange actually occurring far below PEMFC cathode OCP, clearly challenge the current understanding derived from model studies, as well as control experiments performed on thin-film catalyst layers in 0.1 M HClO₄ at room temperature. After establishing a clear correlation between early Pt oxidation and overall PEMFC performance, the predicted transient Pt dissolution associated with the place-exchange mechanism is verified by highly-sensitive electrochemical on-line ICP-MS experiments at 60 °C in 1.0 M HClO₄. Further analysis of the structural data provides first-order time constants for the place-exchange mechanism in both model and PEMFC cathode conditions. In light of these time constants, the limitations of accelerated stress test protocols currently widely used for electrocatalyst materials stability screening is finally demonstrated by means of ultra-fast *operando* WAXS measurements. This new paradigm of Pt oxidation occurring in PEMFC rationalizes both its activity and stability limitations, and paves the way to new mitigation strategies against PEMFC degradation and to the development of durable Pt-based PEMFC electrocatalysts.

Figure 1 showcases the stroboscopic approach used here to collect and process all the *operando* WAXS data and significantly increase signal quality at short exposure time. This approach has been used notably for neutron scattering²⁹⁻³¹, where the required exposure time often exceeds the time constant of investigated processes. Taken as example the fastest measurement performed here (cyclic voltammetry between 0.60 and 1.0 V vs. RHE at 1000 mV s⁻¹), 10,000 WAXS patterns (5 ms exposure time) of the Pt/C catalyst were collected over 75 potential cycles (6 ms temporal resolution). The 75 cycles, supposed periodical in such short overall cycling duration, were merged in a single cycle using

the WAXS measurement timestamp and the cycle period T (here 0.8 s in **Figure 1.a-c**). The resulting single-cycle measurement is largely oversampled, which allows a trade-off between temporal resolution and exposure time by performing local temporal average on the 1D WAXS curves. An arbitrary temporal window of 13 ms was chosen, resulting in the local merging of *ca.* 173 WAXS patterns per point. The as-reconstructed measurement still features high temporal resolution (13 ms) but each WAXS pattern reaches *ca.* 865 ms exposure time (see **Figure 1.d**). As shown in **Figure 1.e**, this operation largely improves the signal-to-noise ratio on the resulting WAXS patterns, allowing structural information to be obtained with much improved combined precision and temporal resolution on stable voltammograms (see **Figure S1** of the **Supplementary Information**). This approach was used for all the *operando* WAXS measurements presented here, collected from either a commercial membrane electrode assembly (MEA, Fuel Cell Store) in a X-ray transparent PEMFC³²⁻³⁵ or a commercial Pt/C catalyst from Johnson Matthey (JM) in a thin-film electrochemical flow cell^{27,28,36} (later referred as 'model conditions') for comparison. The procedure was adapted to the different potential sweep rates used (see **Methods**).

Rietveld refinement of the WAXS patterns was used to extract the lattice constant, crystallite size and (surface) scattering intensity of the Pt phase as a function of the cathode potential (see **Methods**). For convenience, the scattering intensity was converted to surface crystallinity loss *via* normalizing the scale factor by the surface atomic fraction derived from refined Pt crystallite size^{27,37}. As shown in **Figure 1.f** and in agreement with previous observations^{14,27}, both lattice constant values and surface crystallinity of Pt nanoparticles are highly impacted by potential excursions. Contrary to the aforementioned reports, the dependency of these structural parameters on adsorption and surface oxidation processes is here further rationalized by 201-atom models of Pt nanoparticles. As displayed in **Figure 1.g**, the optimized structures when the Pt nanoparticle is (i) covered by hydrogen, (ii) free of adsorbate or (iii) covered with oxygen and their simulated diffractograms (**Figure S2**) qualitatively predict the observed lattice constant expansion during adsorption and scattered intensity decrease during oxidation (see details about theoretical calculations in the **Methods**).

Using these structural descriptors for probing Pt nanocatalyst adsorption and oxidation processes, different key observations can be made from **Figure 2**. Strikingly, the critical potential value triggering the formation of amorphous surface oxides (*i.e.* the formation of subsurface oxygen from the place-exchange mechanism) is identified as being as low as 0.80 V *vs.* RHE from the onset of surface crystallinity loss (dashed line in **Figure 2.b** and **2.d**). This is 300 mV below the generally accepted value of 1.10 V *vs.* RHE from model experiments on Pt(111). Moreover, and as confirmed by the power density curve measured in H₂/O₂ displayed in **Figure 2.a** (see **Methods** and **Figure S3**), this value of critical potential falls right into the centre of practical PEMFC cathode potential range (*i.e.* between 0.60 and 1.0 V *vs.* RHE corresponding to the potential of maximum power density and the open circuit voltage, respectively). In fact, a close comparison between *operando* WAXS data recorded in real PEMFC and in model conditions of the electrochemical flow-cell (**Figure 2.c-d**) highlights the drastic differences between the two systems. Clearly, the data presented support the conclusions reached from previous model experiments regarding the rather low extent of place-exchange below 1.0 V *vs.* RHE in diluted

electrolyte at room temperature (*ca.* 9 % surface crystallinity loss), but the latter reaches *ca.* 30-40 % in PEMFC operated at 80 °C (**Figure 2.c** and **2.d**, depending on cathode's history). These new insights on the central role of place-exchange in PEMFC below the OCP invite to seriously reconsider the underestimated extent of Pt oxidation and associated transient dissolution processes in the practical PEMFC voltage range. Importantly, the near superimposition of the surface crystallinity recovery and the fuel cell polarization curve during the cathodic scan in **Figure 2.b** strongly suggests that, under minimized/suppressed O₂ mass transport limitation, Pt early oxidation controls the PEMFC performance, in agreement with seminal studies on the origin of the overpotential for ORR on Pt^{38,39}. Consequently, the substantial shift of the onset potential for Pt oxidation toward negative potentials in PEMFC must largely contribute to discrepancies between the performance of novel catalyst candidates when tested in a model environment and a practical device^{3,40,41}, in addition to the design of the catalyst layer.

To confirm the effects of such early place-exchange on Pt transient dissolution in conditions relevant to PEMFC, specific Pt dissolution profiles from the commercial Pt/C JM catalyst were investigated by electrochemical on-line ICP-MS for different potential steps (3 min) under different electrolyte concentrations (pH) and temperatures (see **Methods**). The nature and balance of the different anodic and cathodic peaks displayed in **Figure 4.a-b** have been largely discussed previously in the literature^{16,18-21}, and the observed increase of Pt anodic transient dissolution peak intensity (A₁) as the electrolyte concentration and temperature increase was expected^{26,42}. However, it is worth focusing on the novelty of the presented dataset regarding the comparison between potential steps performed within 0.05–0.60–1.23 V vs. RHE and 0.05–0.60–1.0 V vs. RHE. Contrary to the generally accepted trends in low concentration electrolyte and at room temperature where A₁ intensity decreases with the upper potential limit²² (also observed here), the opposite trend is found at higher electrolyte concentration and temperature. Quantitatively, the integration of the Pt dissolution rates in **Figure 4.c-d** reveal the surface state reached at OCP conditions being near 2-fold more damaging to Pt compared to higher voltage. In fact, a recent contribution from Fuchs *et al.* focusing on a Pt(100) extended surface¹⁶ further described the place-exchange as a concomitant growth of two Pt surface oxide types. The anodic dissolution was attributed to the fast nucleation and growth of a first, stripe-like oxide in which Pt is highly unstable against corrosion. The second disordered (hydro)oxide phases, on the contrary, was found to progressively passivate the surface and to disable Pt anodic dissolution at higher potentials while controlling the cathodic dissolution during surface de-passivation. From this subtle interplay between these two oxide species formation, Pt(100) was found the most vulnerable to anodic dissolution at a potential of $E = 1.2$ V vs. RHE in model conditions. The present results indicate this critical potential is necessarily lower for Pt nanoparticles in a PEMFC. Note the associated cathodic dissolution rates C₁ measured from on-line ICP-MS are biased (underestimated) due to enhanced Pt redeposition kinetics at high temperature, which prevent Pt cations from exiting the catalyst layer and reaching the ICP-MS, as suggested by previous reports^{26,42}.

From combined *operando* WAXS and on-line ICP-MS experiments, it is clear that the previously overlooked extent of place-exchange occurring in PEMFC must largely account for both Pt-based

catalysts activity and stability limitations. To further guide new mitigation strategies for catalyst degradation, structural data (surface crystallinity loss) collected during potential steps were analysed to extract the amplitudes and first-order rate constants associated with the place-exchange mechanism below the OCP during Pt oxidation and reduction (see **Methods**, **Figure S4** and **Table S1**).

As shown in **Figure 4**, the Pt oxidation is divided into two steps (the fast and slow steps are labelled step 1 and step 2, respectively) featuring distinct rate constants, while the reduction proceeds in one single fast step. Note the presence of two steps during oxidation is in agreement with previous observations on nanoparticles from Sekizawa *et al.*⁴³ for larger potential excursions, but their possible correspondence with the two oxides types evidenced by Fuchs *et al.*¹⁶ on single crystals is not demonstrated. In general, there is a near constant 3.5-fold increase for both the amplitudes and rate constants of all steps of oxidation and reduction in PEMFC compared to model conditions. In fact, the rate constants for oxidation in PEMFC reach *ca.* 300 ms and 3.6 s for step 1 and step 2, respectively, both contributing equally to near 50 % of the total amplitude of crystallinity loss. This means completing 95 % of the second step of oxidation at OCP will take 3 times these values, *i.e.* more than 10 s. Note the slowest time constants extracted from the fits exceed the '*RC time constant*'⁴⁴ of both electrochemical cells used in this work by at least one order of magnitude (see **Figure S5** and **Table S2**). Such slow temporal evolution questions the concept of accelerated stress tests (ASTs) routinely employed in the literature when screening material stability, as discussed below.

The full power of ultra-fast *operando* WAXS measurement was thus used to benchmark Pt oxidation trends during fast potential cycling in PEMFC. Different potential profiles between 0.60 and 1.0 V vs. RHE were investigated: a 3 s – 3 s square wave (inspired by the standardized AST protocol suggested by the Fuel Cell Technical Team of the U.S Department of Energy, DoE/FCTT²⁵) and triangular waves at different potential sweep rates (5, 10, 100, 500 and 1000 mV s⁻¹), the latter being often found in the literature (see associated voltammograms in **Figures S6-S7**). The results presented in **Figure 5** unambiguously reveal a pronounced effect of the applied potential profile and sweep rate on Pt structural response in PEMFC. Quantifying oxygen surface coverage from lattice constant variation in **Figure 5.a-b**, whereas maximum oxygen surface coverage reached at 1.0 V vs. RHE is nearly equivalent between the square wave and the 5 mV s⁻¹ triangular wave, the maximum oxygen coverage sharply decreases for triangular waves performed at higher sweep rates. Also, the minimum oxygen surface coverage at 0.60 V vs. RHE remains higher for any of the triangular profiles compared to the square wave, with a clear dependence on the sweep rate. The overall Kernel density estimations of the lattice constant values for the different profiles in **Figure 5.c** makes explicit the transition from distinct reduced-oxidized bimodal behaviour toward a partially reduced unimodal state as the sweep rate increases. This naturally translates into the extent of maximum surface crystallinity losses associated to the place-exchange mechanism in **Figure 5.d**. Clearly (and as quantified as 'cycle depth' in **Figure 5.e**), the amount of displaced Pt during a cycle significantly drops for any of the triangular profile applied compared to the square wave, with a clear dependence on the sweep rate. In the frame of quantifying the degradation power of an AST profile, one can define the 'cycle efficiency' being the cycle depth normalized by the

cycle time period. As shown in **Figure 5.f**, the cycle efficiency of the square-wave profile is near 35-, 24-, 10- and >100-fold higher than the triangular waves at 5, 10, 100, > 500mV s⁻¹, respectively.

These observations largely agree with previous conclusions⁴⁵ and support the choice of the Fuel Cell Technical Team of the U.S Department of Energy (DoE/FCTT) in suggesting a square-wave profile as standardized AST protocol. However, it is clear that only 3 s of polarization at 1.0 V vs. RHE is insufficient to reach the steady-state of oxidation. In light of the time constants reported here, 10 s polarization time at the upper potential limit is required to induce the Pt oxidation to be encountered in PEMFC device. The faster reduction process, on the contrary, is largely completed in 3 s, which is consistent with the time constant reported (*ca.* 310 ms). A more rational AST protocol would thus consist in 3 s – 10 s square wave profile between 0.6 and 1.0 V vs. RHE. Finally, the above-conclusions reached from ASTs conducted in PEMFC mostly transpose to model experiments on thin-films at room temperature. Because the time constant of the slowest step in oxidation is found to be 1.15 s, 95 % of the oxidation proceeds in 3.45 s, and the steady-state is not reached during the 3 s – 3 s square wave (see **Figure S8**). In that case, a 3 s – 4 s square wave profile would be more suited, although the practical irrelevance of ASTs conducted at room temperature is here further demonstrated^{26,46}.

CONCLUSIONS

In summary, ultra-fast *operando* WAXS in both PEMFC and model electrochemical environment has been successfully employed to build a new paradigm of Pt oxidation in PEMFC. The major finding is that the onset potential for the place-exchange mechanism in PEMFC is as low as 0.80 V vs. RHE, which is far below the commonly-accepted value and falls right at the centre of PEMFC cathode potential range of operation. Such early Pt oxidation in PEMFC has major consequences for its ORR activity, as the PEMFC performance was found to be highly correlated to Pt surface oxidation recovery during cathodic polarization curve. This must largely contribute for the frequent discrepancies in material activity from model electrochemical environment to PEMFC cathode reported in the literature. Beyond affecting Pt activity, electrochemical on-line ICP-MS experiments confirmed that detrimental Pt degradation routes associated with the place-exchange mechanism, such as anodic and cathodic transient dissolution (previously supposed above PEMFC cathode potential range of operation) actually occur below the open circuit voltage. Finally, determination of first-order time constants associated to the place-exchange mechanism revealed an overall slow process (> 10 s for near-complete oxidation at 1.0 V vs. RHE), which must be considered in the frame of rational ASTs. Efficient Pt oxidation mitigation strategies in PEMFC must consequently be found to significantly improve PEMFC performance and durability. From the material science perspective, disabling Pt oxidation seems an arduous, but not impossible task as atomic decoration or particle encapsulation strategies have already shown promising results^{47,48}. Complementarily, PEMFC system management strategies in the fashion of those currently employed to protect the cathode from high potential excursions during reactant gas starvation or start-up/shut-down of the device could be adapted to potential limits even below the OCP.

METHODS

Materials. Commercial membrane electrode assemblies (MEAs) were purchased from Fuel Cell Store and used in PEMFC without further treatment. The 5-layer, 4.84 cm², MEAs were composed of a 60 wt.% carbon-supported Pt/C catalyst loaded at 0.5 mg_{Pt} cm⁻² for both anode and cathode, a 50.8 μm thick Nafion® NRE-212 membrane, and woven carbon cloth with microporous layer as gas diffusion layers. A 40 wt.% carbon-supported Pt/C was purchased from Johnson Matthey (JM) and used in thin-film electrochemical flow cell without any further treatment.

X-ray transparent fuel cell operation. The MEA was mounted in a house-made X-ray transparent fuel cell largely described in previous contributions³²⁻³⁵. The cell was operated at 80°C with H₂/O₂ or H₂/N₂ at anode/cathode, 65°C dewpoint (52% relative humidity) and 100 mbar backpressure. After a break-in procedure consisting in a 1 h voltage hold at 0.60 V in H₂/O₂, the cathode was purged with N₂ to both fix and minimize ohmic voltage losses. The cell voltage was controlled by a SP-240 potentiostat (Biologic) equipped with a 4 A booster. Prior to any cyclic voltammetry experiment, the high frequency resistance (200 kHz) was measured by means of potentiostatic electrochemical impedance spectroscopy (PEIS), and the potential of the working electrode was dynamically compensated for 85% of the ohmic losses.

Conventional fuel cell operation. The MEA was mounted in a commercial single-cell PEMFC casing (Scribner) and operated at 80°C with H₂/Air or H₂/O₂ at anode/cathode, 80°C dewpoint (100% relative humidity) and 500 mbar backpressure with a house-made test bench. The cell voltage was controlled by a SP-150 potentiostat (Biologic) equipped with a 20 A booster. The break-in procedure was conducted in H₂/Air (313/496 sccm) and consisted of potential cycles between the open circuit voltage (OCV, 10 s), a 100 mV s⁻¹ potential sweep from the OCV to 0.10 V, followed by 1 min hold at 0.10 V. The cycles were repeated for a total duration of 1 h. The oxidant gas was then turned to O₂ and polarization curve was recorded using the staircase potentiostatic electrochemical impedance spectroscopy with a total of 14 potential steps (3 min hold) between the OCV and 0.10 V. The high frequency resistances measured at the end of all steps was used to later correct the potential values from the ohmic losses.

X-ray transparent thin-film electrochemical flow cell operation. 10 μL of an ink suspension composed of 5 mg of 40 wt.% Pt/C catalyst (JM), 3600 μL of 18.2 MΩ ultra-pure water (Millipore), 1446 μL of isopropanol and 20 μL of 5 wt.% Nafion solution (Electrochem. Inc.) were deposited on a 0.196 cm² glassy carbon substrate thus reaching a Pt loading of 20 μg_{Pt} cm⁻². The sample was mounted in a 3-electrode flow cell described in previous contributions^{27,28}. A Pt wire was used as counter electrode and a commercial Ag/AgCl electrode (ET072, eDAQ) as reference electrode. The cell was fed with 0.10 M HClO₄, (Suprapur®, Merck) at a rate of 20 mL min⁻¹ using a peristaltic pump. The electrochemistry was controlled by a SP-300 potentiostat (Biologic). The catalyst was first conditioned using 50 cycles between 0.05 and 1.23 V vs. RHE at 500 mV s⁻¹. The temperature of the room was regulated at 25 °C.

Stroboscopic operando synchrotron wide-angle X-ray scattering (WAXS) measurements. Synchrotron WAXS measurements were performed at ID31 beamline of the European Synchrotron Radiation facility (ESRF) in Grenoble, France. The high energy X-ray beam (77 keV) was focused on the sample through the cells in grazing incidence configuration, and the scattered signal was collected using a Dectris Pilatus CdTe 2M detector. The energy, detector distance and tilts were calibrated using a standard CeO₂ powder and the 2D diffraction patterns were reduced to the presented 1D curves using the pyFAI software package⁴⁹. For a fair comparison between cyclic voltammetry experiments recorded at different potential sweep rates, the chosen temporal resolution for the reconstructed WAXS patterns was kept constant at *ca.* 1/60th of the cycle period *T*. The WAXS measurements were performed on stable cyclic voltammograms. More details on the merging of ultra-fast WAXS data are available on the **Supplementary Information**.

Rietveld refinement of the WAXS patterns. Rietveld refinement of the WAXS patterns was performed to extract the phase structure, crystallite size and lattice parameter using the *Fm3m* structure of Pt and the Fullprof software. The instrumental resolution function was determined by the refinement of a CeO₂ standard sample. Thomson-Cox-Hastings profile function was adopted⁵⁰. The background of patterns was described by an interpolated set of points with refinable intensities.

First-order rate constant determination. The lattice constant and scattered intensity variations during potential steps were fitted using a linear combination of exponential functions of the type:

$$y = y_0 + A_1 e^{-(x-x_0)/t_1} + A_2 e^{-(x-x_0)/t_2}$$

where y_0 and x_0 are the fitted boundary conditions, A_1 and A_2 the fitted amplitude variations, and t_1 and t_2 are the fitted first-order time constants. The two exponential functions were found necessary to capture the oxidation process while only one was sufficient to capture the reduction. More details and numerical values of the fitted parameters can be found in the Supplementary Information.

Electrochemical on-line inductively coupled plasma mass spectrometry. A commercial electrochemical flow cell (BASi, MF-1092, cross-flow cell) was used. The flow cell consists in two glassy carbon disk (3 mm) aligned in series, which are embedded into PEEK material. The first disk was used as counter electrode, and the working electrode is in the direction of the electrolyte flow. 3.4 μL of an ink suspension composed of 5.4 mg of 40 wt.% Pt/C catalyst (JM), 1800 μL of 18.2 M Ω ultra-pure water (Millipore), 723 μL of isopropanol and 29 μL of 5 wt.% Nafion solution (Electrochem. Inc.) were deposited on the 0.071 cm² glassy carbon substrate thus reaching a Pt loading of 20 $\mu\text{g}_{\text{Pt}}\text{cm}^{-2}$. An Ag/AgCl reference electrode was used. The cell was fed with aqueous electrolyte at a rate of 400 $\mu\text{L min}^{-1}$ using a peristaltic pump. The electrochemistry was controlled by a SP-300 potentiostat (Biologic). The electrolyte was either 0.10 M HClO₄, (99.999% trace metal basis, Merck) at room temperature (26 °C), 1.0 M HClO₄ at room temperature (28 °C) or 1.0 M HClO₄ at 60 °C (temperature at the cell outlet). In this last case, the electrolyte was heated prior entering the electrochemical cell (see **Supplementary Information**). The potential shift of the Ag/AgCl reference electrode with temperature was calibrated *in situ* by

measuring the open circuit voltage of the Pt/C working electrode after hydrogen evolution in the cell. The flow cell was connected to an Agilent 7900 ICP-MS equipped with a Micromist/Scott nebulizer. The ^{195}Pt metal ions were detected with 0.1 s integration time per point. Before each measurement, calibration curves were carried out using daily prepared standard solutions of ^{195}Pt (0, 10, 100, 1000 and 10000 ppt). The catalyst was conditioned also using 50 cycles between 0.05 and 1.23 V vs. RHE at 500 mV s^{-1} . The associated Pt electrochemical surface area used for normalization of the ICP-MS data was measured separately using the CO_{ads} stripping technique.

Computational details. Periodic DFT calculations were performed using the Vienna *Ab Initio* Simulation Package (VASP) ^{51,52} within the generalized gradient approximation (GGA) using PBE ⁵³ functional for exchange and correlation potential and projector augmented wave pseudopotentials (PAW) ⁵⁴ with a cut-off energy of 450 eV. 201 Pt atoms truncated-octahedral clusters were computed with up to 192 hydrogen atom and 120 oxygen atoms adsorbed on their facets. H atoms were adsorbed on all hcp sites of the {111} facets and on all residual bridge sites of both edges sites and {110} facets. O atoms were adsorbed on the most stable *fcc* sites of the {111} facets and 4 more O atoms were adsorbed on the {100} ones converging into a threefold-like site. They were set in $2.8 \times 2.8 \times 2.8\text{ nm}^3$ cubic unit cell. The intermolecular facet distances between periodic surfaces were larger than 9 Å. Gamma point calculations were used and structural relaxations were performed on all atoms. The residual forces after structural relaxation were lower than $0.01\text{ eV}/\text{Å}$. Simulated diffraction patterns were obtained by Diamond code.

Declarations

DATA AVAILABILITY

All data supporting the findings in this study are available within the paper and the Supplementary Information. Source data can be provided from the corresponding author on reasonable request.

ACKNOWLEDGEMENTS

The authors thank the ESRF for providing beamtime at ID31 and especially H. Isern and F. Russello for their support at the beamline. The authors also thank the Balard Analysis and Characterization Platform (PAC Balard) facilities for technical support, and especially M. Bigot and N. Donzel for their valuable help with the ICP-MS setup, M. Dupont and F. Lecoœur for support at the hydrogen platform.

AUTHOR CONTRIBUTIONS

Operando X-ray scattering experiments. Conception: R.C., I.M. and J.D.; execution: R.C., I.M., J.D., A.G. and M.S.; analysis: R.C. **Electrochemical on-line ICP-MS experiments.** Conception: C.A.C.-R., D.J. and R.C.; execution: C.A.C.-R., R.C. and A.G.; analysis: C.A.C.-R. **Theoretical model.** Conception, execution and analysis: J.-S.F. **Fuel Cell tests.** Execution: M.S., A.G. and R.C.; analysis: M.S.

R.C., J.D., P.-Y.B., S.C. and D.J. provided funding and supervised the work. R.C. wrote the manuscript with input from all authors.

FUNDING

R.C received financial support from the French National Research Agency through the HOLYCAT project (grant number n° ANR-22-CE05-0007).

COMPETING INTERESTS

The authors declare no competing interests.

References

1. Wang XX, Swihart MT, Wu G (2019) Achievements, challenges and perspectives on cathode catalysts in proton exchange membrane fuel cells for transportation. *Nat Catal* 2:578–589
2. Wang Y, Diaz R, Chen DF, Wang KS, Z., Adroher XC (2020) Materials, technological status, and fundamentals of PEM fuel cells – A review. *Mater Today* 32:178–203
3. Kodama K, Nagai T, Kuwaki A, Jinnouchi R, Morimoto Y (2021) Challenges in applying highly active Pt-based nanostructured catalysts for oxygen reduction reactions to fuel cell vehicles. *Nat Nanotechnol* 16:140–147
4. Borup RL et al (2020) Recent developments in catalyst-related PEM fuel cell durability. *Curr Opin Electrochem* 21:192–200
5. Cullen DA et al (2021) New roads and challenges for fuel cells in heavy-duty transportation. *Nat Energy* 6:462–474
6. Pourbaix M (1974) *Atlas of Electrochemical Equilibria in Aqueous Solutions*. *Mater Sci Forum* doi:10.4028/www.scientific.net/msf.251-254.143
7. Borup R et al (2007) Scientific aspects of polymer electrolyte fuel cell durability and degradation. *Chem Rev* 107:3904–3951
8. De Bruijn FA, Dam VAT, Janssen GJM, Review (2008) Durability and degradation issues of PEM fuel cell components. *Fuel Cells* 8:3–22
9. Dubau L et al (2014) A review of PEM fuel cell durability: Materials degradation, local heterogeneities of aging and possible mitigation strategies. *Wiley Interdiscip Rev Energy Environ* 3:540–560
10. Ruge M et al (2017) Structural Reorganization of Pt(111) Electrodes by Electrochemical Oxidation and Reduction. *J Am Chem Soc* 139:4532–4539
11. Fuchs T et al (2020) Structure dependency of the atomic-scale mechanisms of platinum electro-oxidation and dissolution. *Nat Catal* 3:754–761
12. Smith MC, Gilbert JA, Mawdsley JR, Seifert S, Myers DJ (2008) In situ small-angle X-ray scattering observation of Pt catalyst particle growth during potential cycling. *J Am Chem Soc* 130:8112–8113

13. Gilbert JA et al (2012) In situ anomalous small-angle x-ray scattering studies of platinum nanoparticle fuel cell electrocatalyst degradation. *J Am Chem Soc* 134:14823–14833
14. Martens I et al (2019) Probing the Dynamics of Platinum Surface Oxides in Fuel Cell Catalyst Layers Using in Situ X-ray Diffraction. *ACS Appl Energy Mater* 2:7772–7780
15. Fuchs T et al (2023) Driving Force of the Initial Step in Electrochemical Pt(111) Oxidation. *J Phys Chem Lett* 3589–3593. 10.1021/acs.jpcclett.3c00520
16. Fuchs T et al (2023) Anodic and Cathodic Platinum Dissolution Processes Involve Different Oxide Species. *Angew Chemie Int Ed* 62,
17. Nagy Z, You H (2002) Applications of surface X-ray scattering to electrochemistry problems. *Electrochim Acta* 47:3037–3055
18. Cherevko S et al (2014) Dissolution of noble metals during oxygen evolution in acidic media. *ChemCatChem* 6:2219–2223
19. Sandbeck DJS et al (2020) Particle Size Effect on Platinum Dissolution: Practical Considerations for Fuel Cells. *ACS Appl Mater Interfaces* 12:25718–25727
20. Kasian O, Geiger S, Mayrhofer KJJ, Cherevko S (2019) Electrochemical On-line ICP-MS in Electrocatalysis Research. *Chem Rec* 19:2130–2142
21. Moriau LJ et al (2021) Resolving the nanoparticles' structure-property relationships at the atomic level: a study of Pt-based electrocatalysts. *iScience* 24,
22. Topalov AA et al (2014) Towards a comprehensive understanding of platinum dissolution in acidic media. *Chem Sci* 5:631–638
23. Cho J, Kim H, Oh H, Choi CH (2023) Elucidation of Electrochemically Induced but Chemically Driven Pt Dissolution. *JACS Au*. 10.1021/jacsau.2c00474
24. Cherevko S et al (2015) Dissolution of Platinum in the Operational Range of Fuel Cells. *ChemElectroChem* 2:1471–1478
25. Abdel-Baset T (2017) *The Fuel Cell Technical Team Roadmap*.
https://www.energy.gov/sites/prod/files/2017/11/f46/FCTT_Roadmap_Nov_2017_FINAL.pdf
10.2172/1220127
26. Đukić T et al (2022) Understanding the Crucial Significance of the Temperature and Potential Window on the Stability of Carbon Supported Pt-Alloy Nanoparticles as Oxygen Reduction Reaction Electrocatalysts. *ACS Catal* 12:101–115
27. Chattot R et al (2021) Electrochemical Strain Dynamics in Noble Metal Nanocatalysts. *J Am Chem Soc* 143:17068–17078
28. Chattot R et al (2022) Break-In Bad: On the Conditioning of Fuel Cell Nanoalloy Catalysts. *ACS Catal* 12:15675–15685
29. Iizumi M (1986) Real-time neutron diffraction studies of phase transition kinetics. *Phys B + C* 136:36–41

30. Schillinger B et al (2005) Detection systems for short-time stroboscopic neutron imaging and measurements on a rotating engine. Nucl Instruments Methods Phys Res Sect A Accel Spectrometers Detect Assoc Equip 542:142–147
31. Sheptyakov D et al (2020) Stroboscopic neutron diffraction applied to fast time-resolved operando studies on Li-ion batteries (d-LiNi_{0.5}Mn_{1.5}O₄ vs. graphite). J Mater Chem A 8:1288–1297
32. Martens I et al (2019) X-ray transparent proton-exchange membrane fuel cell design for in situ wide and small angle scattering tomography. J Power Sources 437:226906
33. Martens I et al (2021) Imaging Heterogeneous Electrocatalyst Stability and Decoupling Degradation Mechanisms in Operating Hydrogen Fuel Cells. ACS Energy Lett 6:2742–2749
34. Martens I, Chattot R, Drnec J (2022) Decoupling catalyst aggregation, ripening, and coalescence processes inside operating fuel cells. J Power Sources 521:230851
35. Chattot R et al (2023) Beware of cyclic voltammetry! Measurement artefact in accelerated stress test of fuel cell cathode revealed by operando X-ray diffraction. J Power Sources 555:232345
36. Hornberger E et al (2022) Impact of Carbon N-Doping and Pyridinic-N Content on the Fuel Cell Performance and Durability of Carbon-Supported Pt Nanoparticle Catalysts. ACS Appl Mater Interfaces 14:18420–18430
37. Montejano-Carrizales JM, Morán-López JL (1992) Geometrical characteristics of compact nanoclusters. Nanostructured Mater 1:397–409
38. Nørskov JK et al (2004) Origin of the overpotential for oxygen reduction at a fuel-cell cathode. J Phys Chem B 108:17886–17892
39. Stamenkovic VR et al (2007) Improved oxygen reduction activity on Pt₃Ni(111) via increased surface site availability. Science 315:493–497
40. Stephens IEL, Rossmeisl J, Chorkendorff I (2016) Toward sustainable fuel cells. Science 354:1378–1379
41. Ly A, Asset T, Atanassov P (2020) Integrating nanostructured Pt-based electrocatalysts in proton exchange membrane fuel cells. J Power Sources 478:228516
42. Cherevko S, Topalov AA, Zeradjanin AR, Keeley GP, Mayrhofer KJ (2014) J. Temperature-Dependent Dissolution of Polycrystalline Platinum in Sulfuric Acid Electrolyte. Electrocatalysis 5:235–240
43. Sekizawa O et al (2018) Key Structural Transformations and Kinetics of Pt Nanoparticles in PEFC Pt/C Electrocatalysts by a Simultaneous Operando Time-Resolved QXAFS–XRD Technique. Top Catal 61:889–901
44. Bard AJ, Faulkner LR (2001) *Electrochemical Methods: Fundamentals and Applications*. *Electrochemical Methods: Fundamentals and Applications*. John Wiley & Sons, Inc.
45. Stariha S et al (2018) Recent Advances in Catalyst Accelerated Stress Tests for Polymer Electrolyte Membrane Fuel Cells. J Electrochem Soc 165:F492–F501
46. Dubau L, Maillard F (2016) Unveiling the crucial role of temperature on the stability of oxygen reduction reaction electrocatalysts. Electrochem commun 63:65–69

47. Xiao F et al (2022) Atomically dispersed Pt and Fe sites and Pt–Fe nanoparticles for durable proton exchange membrane fuel cells. *Nat Catal* 5:503–512
48. Zhao Z et al (2022) Graphene-nanopocket-encaged PtCo nanocatalysts for highly durable fuel cell operation under demanding ultralow-Pt-loading conditions. *Nat Nanotechnol* 17:968–975
49. Ashiotis G et al (2015) The fast azimuthal integration Python library: PyFAI. *J Appl Crystallogr* 48:510–519
50. Thompson P, Cox DE, Hastings JB (1987) Rietveld Refinement of Debye-Scherrer Synchrotron X-ray Data from A1203. *J Appl Crystallogr* 20:79–83
51. Kresse G, Furthmüller J (1996) Efficiency of ab-initio total energy calculations for metals and semiconductors using a plane-wave basis set. *Comput Mater Sci* 6:15–50
52. Kresse G, Furthmüller J (1996) Efficient iterative schemes for *ab initio* total-energy calculations using a plane-wave basis set. *Phys Rev B* 54:11169–11186
53. Perdew JP, Burke K, Ernzerhof M, Ernzerhof M (1996) Generalized gradient approximation made simple. *Phys Rev Lett* 77:3865
54. Kresse G, Joubert D (1999) From ultrasoft pseudopotentials to the projector augmented-wave method. *Phys Rev B* 59:1758–1775

Figures

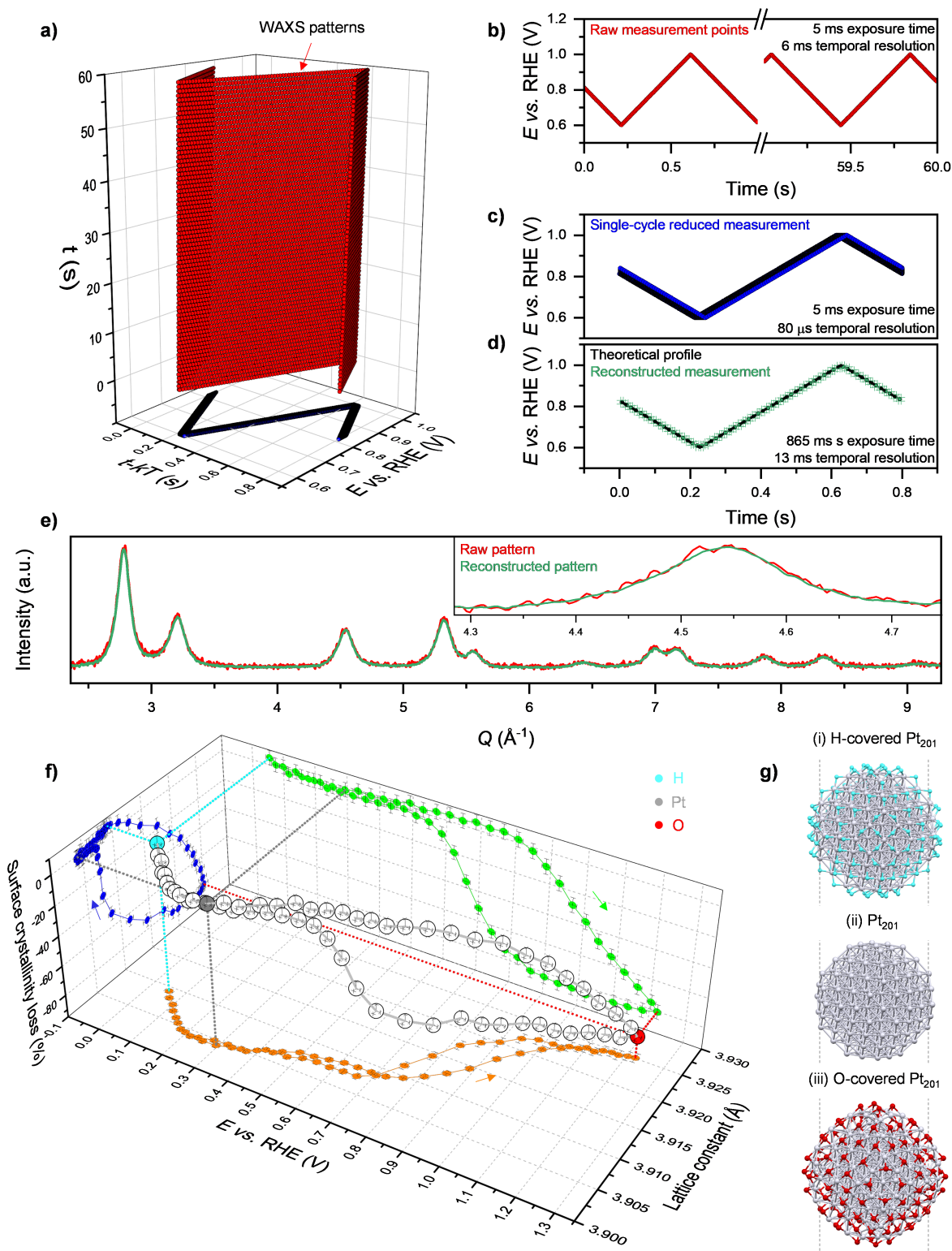


Figure 1

Stroboscopic *operando* WAXS to capture Pt cathode catalyst microstructural properties with high resolution during (fast) potential cycling. a) 3D plot of the 10,000 WAXS measurements timestamp t as a function of the electrode potential and the period-corrected timestamp (T being the time period of a cycle and k the cycle number measured over 75 cycles between 0.60 and 1.0 V vs. RHE at 1000 mV s^{-1}). b) Corresponding applied electrode potential profile and WAXS measurement distribution as a function

of time. c) Reduction of the 10,000 WAXS measurements in one single potential cycle. d) Theoretical single-cycle reduced potential profile (dashed line) and reconstructed measurements obtained by applying moving average on the WAXS patterns. e) Signal-to-noise reduction associated to the increased exposure time on the reconstructed vs. raw WAXS patterns plotted as a function of the momentum transfer Q . f) 3D plot of the operando WAXS measurement during cyclic voltammetry experiment at 20 mV s^{-1} with associated 2D projections showing the relations between the electrode potential, Pt lattice constant and surface-fraction-normalized scattering intensity variations. Three measurement points highlighted in (i) blue, (ii) grey and (iii) red indicate where the particle is covered with hydrogen, mostly free of adsorbate and covered with oxygen, respectively. g) Three models of 201-atom Pt nanoparticle with optimized structure when (i) covered with hydrogen, (ii) free of adsorbate and (iii) covered with oxygen. The dotted lines in g) guide the eye catching the lattice expansion during the formation of adsorbates.

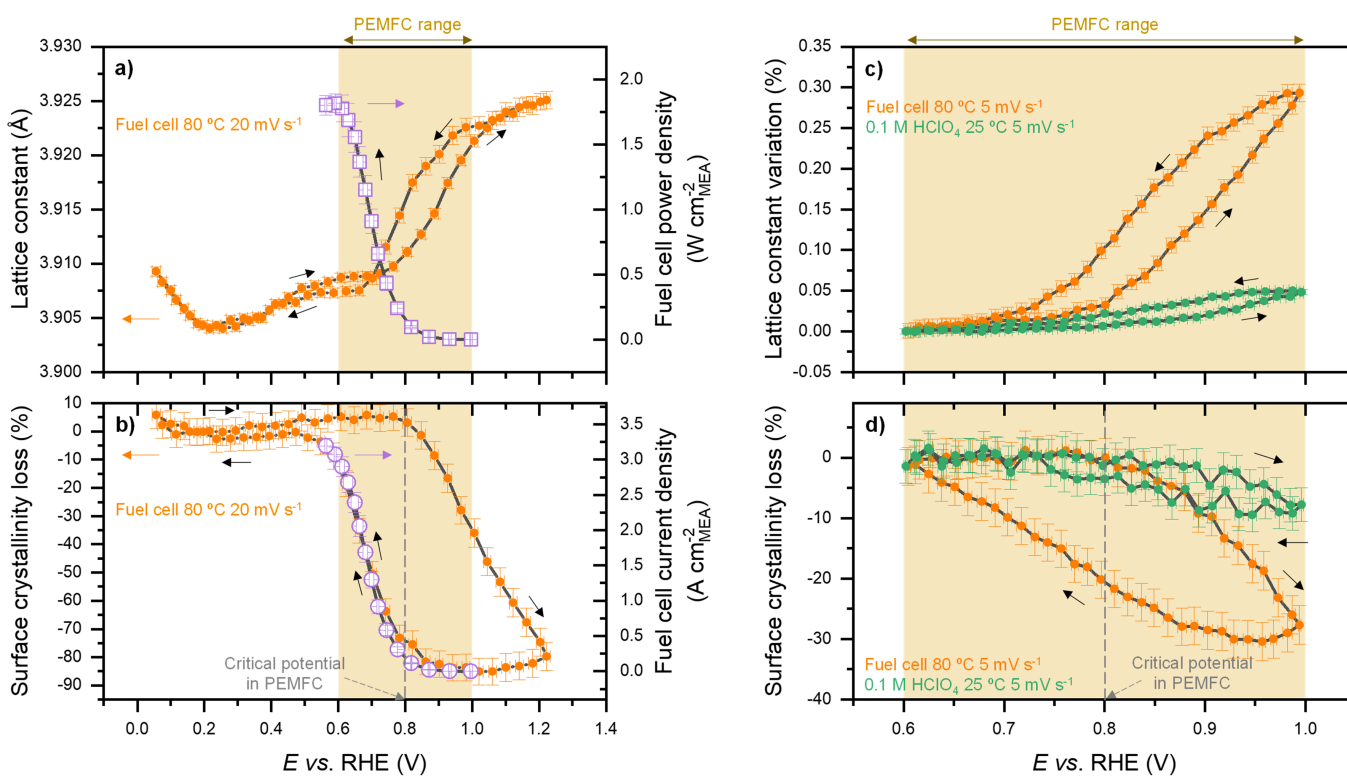


Figure 2

Revealing the critical potential for place-exchange being at the centre of PEMFC cathode voltage range.

a) Pt lattice constant variations and b) surface-fraction-normalized scattering intensity variations during cyclic voltammetry experiment in PEMFC between 0.05 and 1.23 V vs. RHE at 20 mV s^{-1} . c) Pt lattice constant relative variations and d) surface-fraction-normalized scattering intensity variations during cyclic voltammetry experiment in PEMFC (orange markers) and in electrochemical flow cell fed with 0.1 M HClO_4 (green markers) between 0.60 and 1.0 V vs. RHE at 5 mV s^{-1} . The fuel cell for *operando* WAXS was operated at 80°C , H_2/N_2 at anode/cathode, 65°C dewpoint, 100 mbar backpressure, and the electrochemical flow-cell at controlled room temperature of 25°C . The fuel cell power density (purple

square) and current density (purple dots) plotted in a) and b), respectively, were measured in a separated dedicated experiment on similar MEA and the cell was operated at 80 °C, H₂/O₂, 313/496 sccm at anode/cathode, 80 °C dewpoint, 500 mbar backpressure after 3 min of stabilization per point. The cell voltage was corrected at each point by the cell high frequency resistance. The orange boxes in all the plots represent the PEMFC practical voltage range between 0.60 and 1.0 V vs. RHE, corresponding to the voltage of maximum power density and the open circuit voltage, respectively, as shown in a). In b) and d) the surface crystallinity losses are normalized by their values at $E = 0.4$ V vs. RHE and $E = 0.60$ V vs. RHE, respectively.

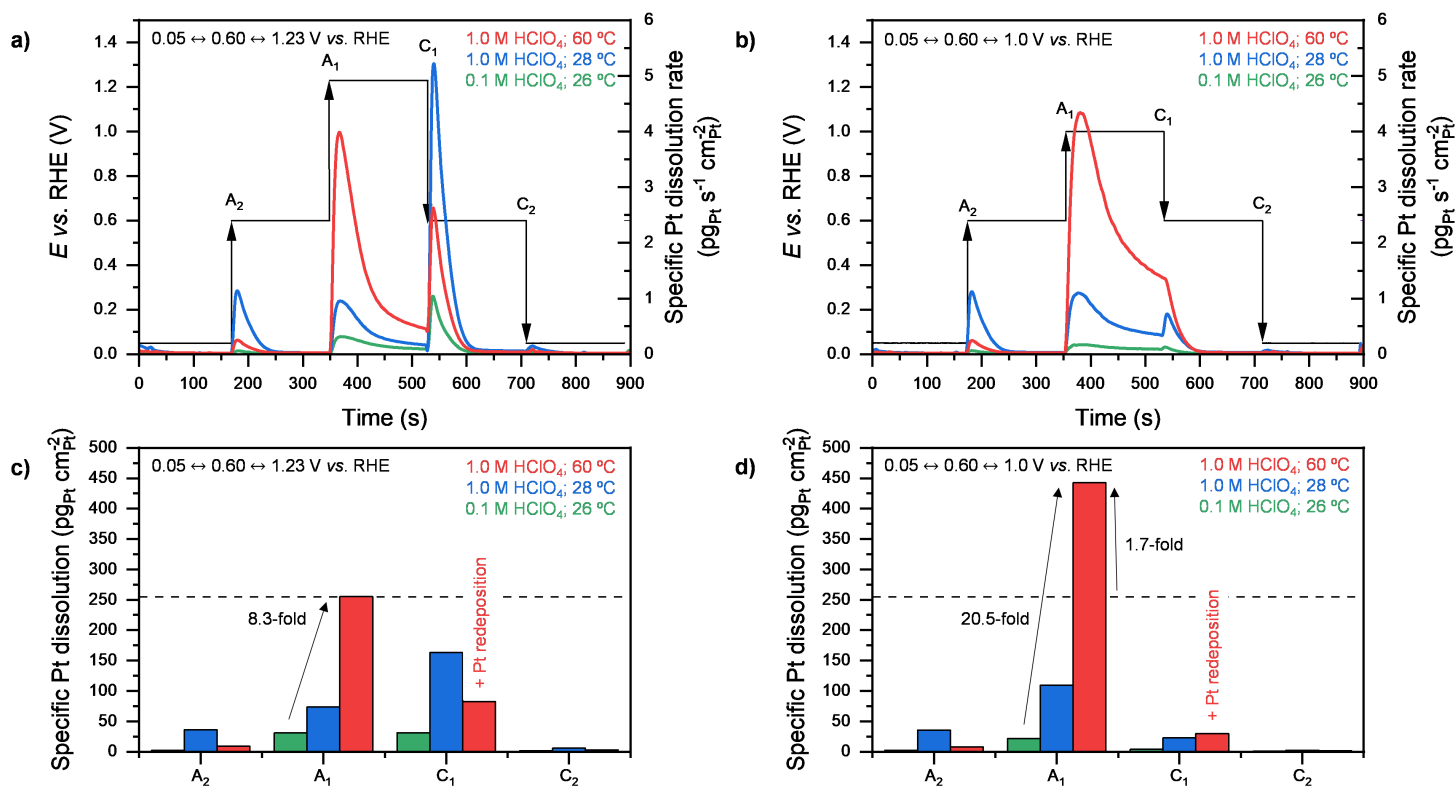


Figure 3

Transient specific Pt dissolution profiles from model to PEMFC-like conditions revealed by electrochemical on-line ICP-MS experiments with temperature control. Specific Pt dissolution profiles recorded a) outside (0.60 – 1.23 V vs. RHE) and b) inside (0.60 – 1.0 V vs. RHE) PEMFC cathode potential range during 3 min hold potential steps from 0.05 V vs. RHE under different conditions of electrolyte concentration (pH) and temperature. c)-d) Total dissolved Pt during the different anodic (A_x) and cathodic (C_x) peak contributions from panel a) and b), respectively. The ICP-MS measurements were performed on a commercial 40 wt.% Pt/C catalyst from Johnson Matthey (JM) and the electrode loading was 20 μg_{Pt} cm⁻².

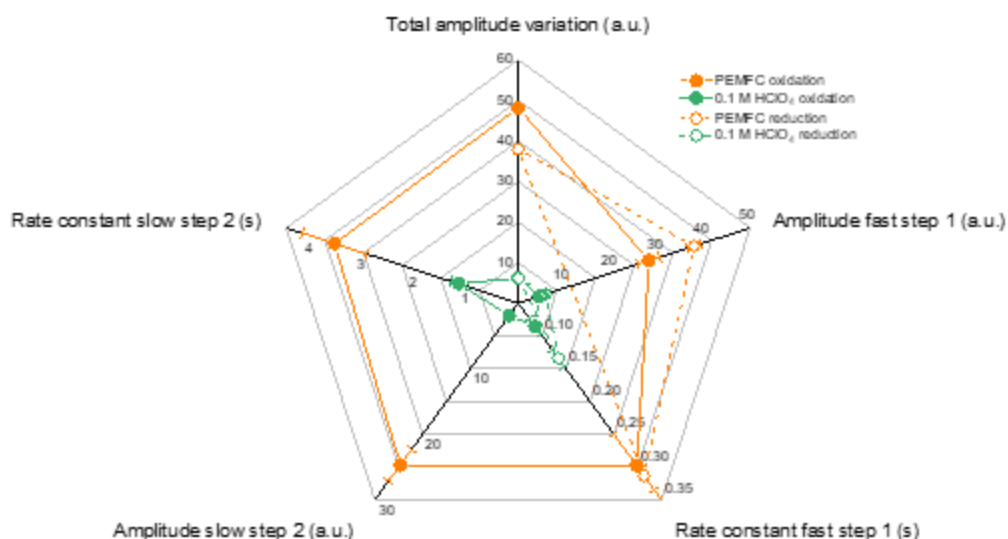


Figure 4

Determination of first-order rate constants and amplitudes associated with the place-exchange mechanism in both PEMFC and model electrochemical environments. Surface crystallinity loss from *operando* WAXS data recorded during potential steps between 0.60 to 1.0 V vs. RHE and 1.0 to 0.60 V vs. RHE were fitted using a linear combination of one or two exponential functions. Two functions were found necessary to capture two distinct steps during oxidation: a fast process (step 1) and a slow process (step 2). This was not found necessary during the reduction, which occurs in one single fast step (step 1). The radar chart allows easily comparing the fitted parameters from one electrochemical environment to the other: the total amplitude variations of surface crystallinity loss also with the amplitudes and first-order rate constants associated to the different steps. The filled and hollow markers correspond to the oxidation and reduction data, respectively. The error bars represent the standard deviations associated to the fitted parameters.

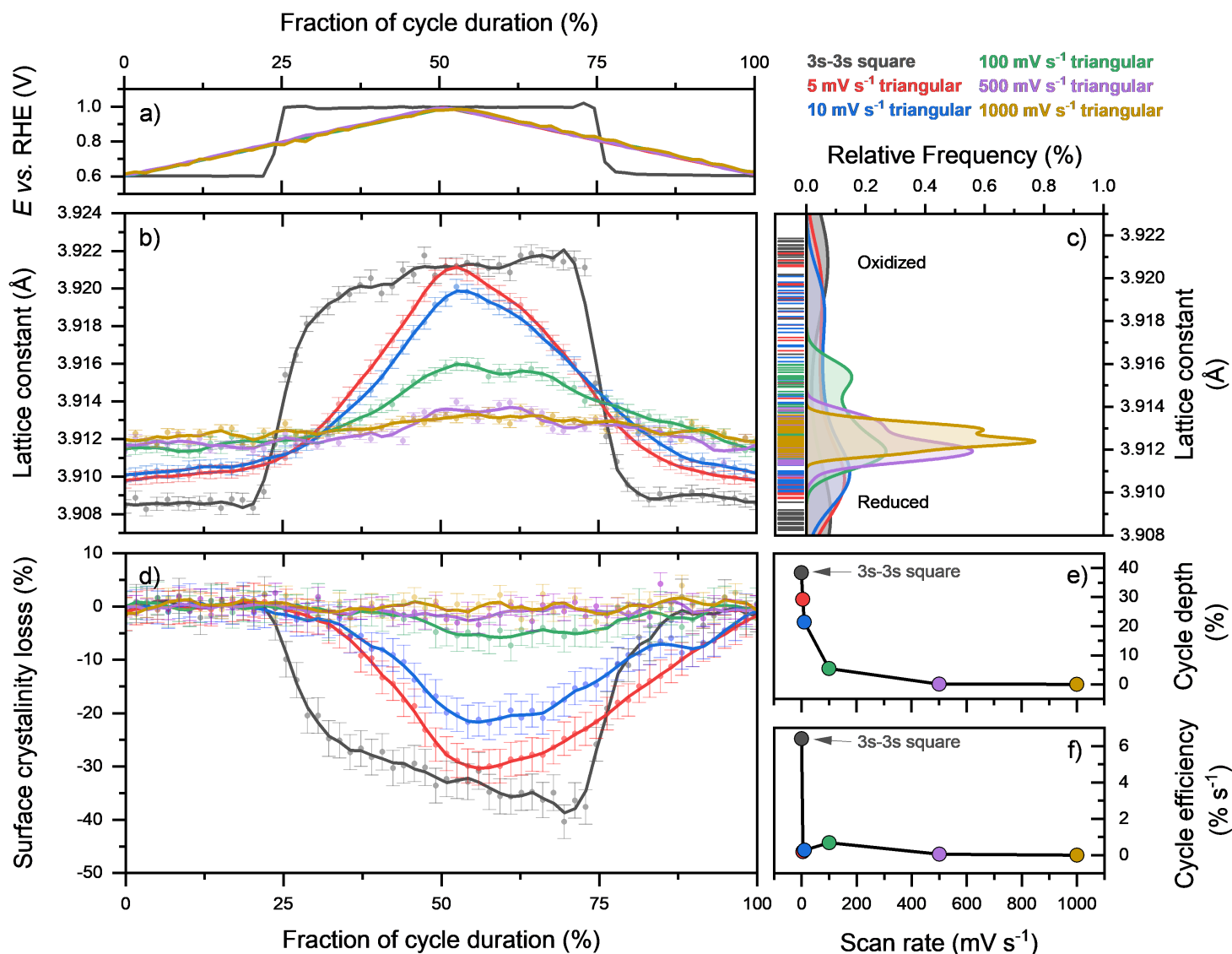


Figure 5

Outpacing Pt oxidation in fuel cell catalyst layer during accelerated stress tests. a) Reconstructions of the applied potential cycle profiles between 0.60 and 1.0 V vs. RHE: 3 s – 3 s square wave and triangular waves at 5, 10, 100, 500 and 1000 mV s⁻¹, b) lattice constant variations with c) associated Kernel density distribution. d) surface-fraction-normalized scattering intensity variations. e) Maximum of surface crystallinity loss induced by each potential profile type (cycle depth) and f) rate of surface crystallinity loss induced by each potential cycle profile (cycle efficiency). The voltage was dynamically corrected by the cell high frequency resistance.

Supplementary Files

This is a list of supplementary files associated with this preprint. Click to download.

- [SIPtOxOCP.docx](#)